Submitted to CJCP, 10/15/2021, revised 11/2/2021

Assessing Density Functionals for Describing Methane Dissociative Chemisorption on Pt(110)-(2×1) Surface

Fenfei Wei,[1] Egidius W. F. Smeets,[2] Johannes Voss,[3] Geert-Jan Kroes,[2] Sen Lin[1,*], and Hua Guo[4,*]

[1]State Key Laboratory of Photocatalysis on Energy and Environment, College of Chemistry, Fuzhou University, Fuzhou 350002, China

[2]Leiden University, Leiden Institute of Chemistry, Einsteinweg 55, 2333 CC, Leiden, The Netherlands

[3]SUNCAT Center for Interface Science and Catalysis, SLAC National Accelerator Laboratory, 2575 Sand Hill Road, Menlo Park CA, 94025, USA

[4]Department of Chemistry and Chemical Biology, University of New Mexico, Albuquerque, New Mexico 87131, USA

*: corresponding authors: slin@fzu.edu.cn, hguo@unm.edu

Abstract

In this work, we explore the suitability of several density functionals with the generalized gradient approximation (GGA) and beyond for describing the dissociative chemisorption of methane on the reconstructed Pt(110)-(2×1) surface. The bulk and surface structures of the metal, methane adsorption energy, and dissociation barrier are used to assess the functionals. A van der Waals corrected GGA functional (optPBE-vdW) and a meta-GGA functional with van der Waals correction (MS PBEl-rVV10) were selected for AIMD calculations of the sticking probability (S_0). Our results suggest that the use of these two functionals may lead to a better agreement with existing experimental results, thus serving as a good starting point for future development of reliable machine-learned potential energy surfaces for the dissociation of methane on the Pt(110)-(2×1) surface.

1. Introduction

Dissociative chemisorption (DC) of methane (CH_4) and its deuterated isotopologues on metal surfaces has served as a prototype in understanding gas-surface reaction dynamics.[1-5] Molecular beam studies have revealed that the DC process is typically direct and activated, i.e., the sticking probability (S_0) usually increases monotonically with increasing incident kinetic energy (E_i).[6-9] More interestingly, putting energy in different vibrational modes of the impinging molecule is shown to lead to different activation efficacies, resulting in vibrational mode specificity (and bond selectivity).[10-15] In some cases, vibrational energy is more efficient in breaking the chemical bond than translational energy.[12] These experimental observations have largely been reproduced by theory, using either ab initio molecular dynamics (AIMD) or dynamics calculations on various potential energy surfaces (PESs) derived from density functional theory (DFT) calculations.[16-42] However, a quantitative characterization of the DC dynamics requires an accurate description of the reaction barrier, which is difficult to achieve with the current generation of standard density functionals (DFs) based on the generalized gradient approximation (GGA).[5] As a result, it is desirable to assess the performance of these and other DFs and to design more accurate ones.

Recently, a concerted effort has been made to find DFs that allow measured molecular beam sticking probabilities to be reproduced with chemical accuracy (errors < 1 kcal/mol) for systems in which methane interacts with a metal surface.[30-32, 34, 36, 43] This goal has been achieved for methane interacting with the Ni(111),[31] Pt(111),[32] and Pt(211) surfaces[32, 43] using the specific reaction parameter (SRP) approach to DFT.[5, 44] Essentially, an SRP DF is a weighted average of an "attractive" DF that overestimates the reactivity (e.g., PW91[45] or the PBE DF[46] designed to

substitute it[46]) and a "repulsive" DF that underestimates the reactivity (e.g., RPBE[47]) that yields reaction barriers of chemical accuracy.[5] Indeed, the first SRP-DF[44] was a simple weighted average of PW91 and RPBE. For methane interacting with metal surfaces it turned out to be necessary[30-32] to use a van der Waals correlation functional (vdW-DF[48]) rather than a GGA correlation functional to obtain a SRP-DF, due to the rather strong van der Waals interaction in this class of systems.[31, 32]

Studies on methane-metal surface systems pointed to a considerable degree of transferability of the SRP-DF among chemically related systems.[5] Specifically, the SRP-DF for methane + Ni(111) also turned out to be an SRP-DF for methane + Pt(111),[32] with these metals belonging to the same group of the periodic system. The same SRP-DF[31] also describes CH_4 + Ir(111) quite accurately.[40] More relevant to the present paper, transferability also occurs among systems in which methane interacts with different low index faces of the same metal: The SRP-DF for CH_4 + Pt(111) worked well for CH_4 + Pt(211),[32] and the (same) SRP-DF for CH_4 + Ni(111) also quite accurately describes sticking of CH_4 to Ni(211).[39]

However, a number of examples has emerged in which SRP functionals did not exhibit transferability among chemically related systems. One such example is the DC of methane on the kinked Pt(210) surface, where the calculated S_0 are shifted relative to the experimental values by more than 10 kJ/mol.[36] The shift found for the reconstructed Pt(110)-(2×1) surface is even larger (~20 kJ/mol).[49] These failures are surprising given the high accuracy exhibited by one and the same DF (the SRP32-vdW DF) in characterizing methane DC on Pt(111) and Pt(211)[32, 43, 50] and Ni(111)[31] and Ni(211).[39] A possible cause that has been suggested for the poor performance of this DF for methane + Pt(110)-(2×1), which system is the focus of the present work, is its failure at accurately predicting the structure of the reconstructed Pt surface.[49] Specifically, dynamics

calculations on H_2 + Cu(111) and Cu(100) have shown that variations in the interlayer distances in the surface region of the metal may have a large effect on the molecule-metal surface interaction,[51, 52] suggesting that it is important to get the surface structure right.

The Pt(110)-(2×1) surface is of great interest as experimental studies have shown that the S_0 at low incident energies actually increases with decreasing incident energy,[53, 54] in sharp contrast to the activated behavior usually observed for methane DC on metals. Such a negatively activated regime is most likely attributable to a precursor-mediated mechanism, in which the impinging methane molecule is trapped on the surface for a significant period of time,[55-57] but this hypothesis requires theoretical confirmation. For such events, the AIMD approach to the DC dynamics is inefficient because of the long time nature of the dynamics.[29, 38, 41] Instead, an analytical PES based on the DFT data can be constructed using machine learning, which will accelerate the dynamics calculations significantly.[37, 42] However, constructing a PES is often a demanding task[58] and it is highly desirable to identify an accurate DF beforehand, which despite extensive DFT studies,[49, 59-63] has not been settled.

It is well established that pure GGA-type DFs are often incapable of a simultaneously accurate characterization of the molecule-surface interaction and the structure of the metal surface.[64] Furthermore, as already mentioned, the molecule-surface interaction energy is also strongly dependent on the structure of the surface (e.g., on the interlayer distances in the surface region of the metal).[51, 52] A notable problem of the SRP-32-vdW functional, which contains GGA exchange,[31] is that it overestimates the Pt lattice constant, and, perhaps as a result, it also fails to yield an accurate description of the parameters governing the interlayer distances in the surface region of Pt(110)-(2×1).[49] It should therefore be of interest to perform tests on this system with DFs that are capable of an accurate description of metal structure while also being capable of a

simultaneously accurate description of the molecule-surface interaction. In this context it is also of interest to note that recent quasi-classical trajectory (QCT) calculations using a reactive force field based on DFT calculations with the PBE DF[63] led to similar underestimation of measured S_0 for CHD_3 + Pt(110) as obtained earlier with the SRP32-vdW-DF.[49]

Meta-GGA DFs,[65] for which the exchange-correlation energy additionally depends on the kinetic energy density τ, are in principle capable of meeting these demands. This is particularly true for the so-called made-simple (MS) meta-GGA DFs.[66, 67] In these functionals, the value of τ is used to identify regions in space that are metallic and regions in which electrons form single bonds, which occur in molecules and in molecular fragments bonding to metals. An exchange enhancement factor is then set up that is capable of representing a GGA exchange functional that is accurate for metals in the former regions and of representing a GGA that is good for molecules in the latter regions.[66, 67] Sun and co-workers first developed the MS0 DF[66] and the MS1 and MS2 DFs,[67] where the MS0 DF can be classified as a non-empirical DF and the MS1 and MS2 DFs as semi-empirical DFs.[68] Essentially, the parameters in the MS1 and MS2 DFs were fit to formation energies of molecules and to gas phase reaction barrier heights, for which these two DFs show a good performance.[67] The MS2 functional also has shown a reasonable performance on chemisorption energies,[69-72] and an excellent performance on lattice constants and cohesive energies of strongly bound solids.[73] However, the MS2 DF performed less well at reproducing reaction barriers heights for DC of molecules on metal surfaces in the SBH10 database than a DF incorporating GGA exchange and van der Waals correlation,[74] i.e., the BEEF-vdW DF.[69]

Because the MS2 DF seemed to perform rather poorly at computing barriers for DC on metals, a subclass of MS type functionals (MS-PBEl, MS-B86bl, and MS-RPBEl) was developed

for this purpose, and tested on H_2 DC on (111) faces of Cu, Ag, Au, and Pt.[75] All three DFs gave a chemically accurate description of the DC of H_2 on Cu(111), while also providing an accurate description of the DC of H_2 on Ag(111).[75] The lattice constants computed for the four metals mentioned exhibited[75] an accuracy similar to that obtained with the PBEsol DF, which was developed specifically for the solid state.[76] Furthermore, the MS-RPBEl DF[75] was shown to yield a better description of the DC of HCl on Au(111)[77] and of O_2 on Al(111)[78] than the RPBE GGA DF.[47] The three new MS exchange-correlation DFs were also tested[79] with their correlation parts replaced with the revised Vydrov-van Voorhis correlation functional[80] (rVV10),[81] which yields an approximately correct description of the van der Waals attraction. While it was found that the overall description of the metal lattice constants was not as good as obtained with the MS functionals with their original correlation functional in place, overall the good description of the DC of H_2 on the (111) faces of Cu, Ag, Au, and Pt was retained. This makes these functionals of interest to the description of the DC of methane on metal surfaces, which, as discussed above, requires an approximately correct description of the van der Waals interaction.[30, 31] We will therefore also test the performance of this type of DFs (i.e., the subclass of new MS DFs augmented with the rVV10 correlation) on the DC of methane on reconstructed Pt(110).

Meta-GGA DFs are not the only DFs of interest in the context of this work. Previous work has shown that semi-empirical DFs[82, 83] containing GGA exchange but non-local van der Waals correlation (i.e., vdW-DF[48]) are capable of a good description of solids,[83] even though they were developed to reproduce non-covalent intermolecular interactions, which they describe with chemical accuracy.[82, 83] For example, the optPBE-vdW DF[82] describes solids with an accuracy[83] comparable to that of the PBE DF.[46] Compared to MS2,[67] the optPBE-vdW DF is somewhat less accurate for barriers for gas phase reactions,[5] and more accurate for physisorption of molecules on

metals,[71] but less accurate for molecular chemisorption and DC reaction energies on metals.[70, 71] However, the optPBE-vdW DF has recently been shown to yield a chemically accurate description of the DC of H_2 on Cu(111)[84, 85] and on Cu(100)[85] and Cu(110).[85] This would suggest that DFs incorporating GGA exchange are capable of a simultaneously accurate description of the metal and of the DC of molecules on metal surfaces, as long as they incorporate non-local (van der Waals) correlation. Of course, for DC of methane on metals such DFs have the added advantage that they have the van der Waals attractive interaction already built into them. We will therefore also test the performance of this type of DFs on the DC of methane on reconstructed Pt(110).

The goal of this work is to identify DFs that may form a good starting point for developing machine learned PESs for the DC of methane on missing row reconstructed Pt(110). In this work we therefore examine the fitness of several GGA, GGA exchange + vdW correlation, meta-GGA, and meta-GGA + rVV10 correlation DFs for describing the DC in this system. We test a number of DFs of these sub classes on the lattice constant of the solid, the structure of the reconstructed surface, and the site specific dissociation barrier for the system of interest. For two selected DFs, optPBE-vdW[82] and MS PBEl-rVV10,[79] exploratory AIMD calculations are carried out and rough estimates of the S_0 (i.e., with still fairly large statistical errors) are computed at two incident energies, and compared with experiment.[49] Our results suggest that the use of both DFs tested may lead to good agreement with existing experimental results if a sufficient amount of trajectories are computed so that results can be obtained with small enough statistical error bars, which would allow a definitive comparison to the existing experiments.[49] The two DFs tested are therefore a good starting point for studies aimed at developing reliable machine-learned PESs for further theoretical studies of the DC of methane on Pt(110)-(2×1).

2. Method

DFT calculations were conducted using the Vienna *Ab initio* Simulation Package (VASP).[86-88] The electronic wave functions were expanded into plane waves up to a cutoff energy of 38594.1 kJ/mol and the wave functions of the ionic core electrons were approximated by the projector augmented-wave (PAW) method.[89] The Brillouin zone was sampled using 3 × 3 × 1 Monkhorst-Pack *k*-point grids for the optimization.[90] A 1 × 3 unit cell of Pt(110)-(2×1) in the xy-plane was used under periodic boundary conditions in all calculations. In the seven atomic layers, only the top four atom layers were relaxed. A vacuum distance of 20 Å was employed along the z-direction to avoid interactions between the periodic images. The electron density for the atomic ground states converged with a 9.648×10^{-4} kJ/mol total energy threshold, and the structures were optimized until the maximum force acting on any ion was less than 1.930 kJ/mol·Å^{-1}. The climbing image nudged elastic band (CI-NEB) method[91] was used to search for transition states (TS), and the maximum force acting on any ion for each image was less than 1.930 kJ/mol·Å^{-1}. The adsorption energy (E_{ads}), the activation energy (E_a), the barrier height (the TS energy relative to the asymptote, E_b), and the reaction energy (ΔE) are defined as follows:

$$E_{ads} = E_{\mathrm{CH_4/Surface}} - E_{\mathrm{Surface}} - E_{\mathrm{CH_4}}, \quad (1)$$

$$E_a = E_{\mathrm{TS}} - E_{\mathrm{IS}}, \quad (2)$$

$$E_b = E_{\mathrm{TS}} - E_{\mathrm{Surface}} - E_{\mathrm{CH_4}}, \quad (3)$$

$$\Delta E = E_{\mathrm{FS}} - E_{\mathrm{IS}}, \quad (4)$$

where $E_{\mathrm{CH_4/Surface}}$, E_{Surface}, $E_{\mathrm{CH_4}}$ are the energy of the adsorption structure of the complete

system, of the bare Pt(110)-(2×1) surface, and of the CH_4 molecule in the gas phase, respectively. E_{IS}, E_{TS}, E_{FS} are the energy of the initial adsorption state (IS), the TS and the final state (FS) of the complete system in the CI-NEB calculation. Note that E_{IS} is equal to $E_{\mathrm{CH_4/Surface}}$ as here defined. We also define E_{ads}^{zpe} and E_{a}^{zpe} as the zero-point energy corrected adsorption energy and activation energy, respectively. In the present context of a comparison to molecular beam sticking probabilities measured at hyperthermal energies, the barrier height is the most relevant quantity for judging the quality of the tested DFs for the system of interest. The activation energies mentioned would be more relevant to the description of DC under thermal conditions.

The following DFs were tested in the DFT calculations: three GGA type DFs (PBE,[46] RPBE,[47] and PBEsol,[76]), ten DFs consisting of GGA exchange and van der Waals correlation or corrections (PBE-D3,[92] vdW-DF/vdW-DF2,[48, 93] optPBE-vdW/optB86b-vdW/optB88-vdW,[82, 83] TS/TS-SCS,[94, 95] BEEF-vdW,[69] and SRP32-vdW[31]), three MS meta-GGA DFs (MS-PBEl, MS-RPBEl, and MS-B86bl),[75] and three MS meta-GGA exchange DFs combined with rVV10 correlation (MS-PBEl-rVV10, MS-RPBEl-rVV10, and MS-B86bl-rVV10).[79] The MS meta-GGA exchange DFs are used with PBE-like, RPBE-like, and B86b-like expressions for the exchange functional, respectively.[75]

In the AIMD simulation, the same DFT-model as described above was used, but only the optPBE-vdW and MS-PBEl-rVV10 DFs were tested in the on-the-fly calculation of trajectories. To compare to the recent experimental study,[49] we have chosen CHD_3 as the impinging molecule. The initial conditions of the trajectories, including the surface temperature (T_s) and the incident energy and angle, were also selected to mimic the experimental conditions. Specifically, the temperature T_s of Pt(110)-(2×1) surface was set at 650 K and the surface coordinates and momenta

obtained after equilibration under the NVE ensemble for 4 ps with a 1 fs time step were used to generate the initial conditions for the dynamics calculations. To accommodate thermal expansion, the 0 K lattice constant was expanded by 1.005.[31, 32] The QCT method was used as implemented in a user-modified version[96] of the VENUS code.[97] The distance of the molecular center of mass (COM) of CHD_3 to the surface was initialized at 6 Å, where the surface was taken to be at the average height (z-coordinate) of the ridge Pt atom. The vibrational temperature characterizing the Boltzmann distribution of CH_4 was obtained from the nozzle temperature (T_N = 550 and 650 K),[49] and the zero point energy was set as the lowest vibrational energy. Two incident translational energies (E_i = 106.8 and 124.6 kJ/mol) and normal incidence were used and the AIMD trajectories were propagated by using the Verlet algorithm with a time step of 1 fs. Considering the high computational cost, 100 and 50 AIMD trajectories were propagated for the optPBE-vdW and MS-PBEl-rVV10 DFs, respectively, for each incident translational energy. Each trajectory is propagated until either the molecule is scattered or dissociated. A trajectory was considered reactive if the C-H bond distance (or one of the C-D bond distances) exceeded 2.2 Å and scattered when the CHD_3 COM was more than 6.0 Å above the ridge Pt atoms. If a trajectory led to neither dissociation nor scattering after the 2 ps propagation time, the molecule was considered trapped.

It should be noted that with the number of atomic layers employed the reaction barrier heights are not yet converged to within 1 kcal/mol. This would require calculations with a slab consisting of at least nine atomic layers,[49] which was deemed to expensive for the AIMD studies, which are meant to represent an exploratory study. However, we do expect that the differences between barrier heights computed with different DFs can be accurately computed with the present computational set-up, so that a good candidate DF can be selected for later studies to obtain a machine-learned PES. Identification of such DFs is the main purpose of this work.

3. Results and discussion

3.1 Structure of the Pt(110)-(2×1) surface layers

As discussed above, the structure of the reconstructed Pt(110)-(2×1) surface is expected to impact the PES of the gas-solid reaction system and ultimately the sticking probability. As shown in Figure 1a, the missing row reconstruction of the Pt(110) surface leads to ridge, facet, and valley surface atoms, resulting in different Pt coordination numbers of 7, 10 and 11, respectively. The ridge atoms have relatively strong interactions with the bottom atoms because of their low coordination number. As a result, the interaction between the Pt atoms on the surface manifests itself in lateral pairing and buckling, resulting in varying inter-layer spacings.[98] We have investigated the influence of the DF on the Pt lattice using a slab of 7 atomic layers with a 1×3 supercell (Figure 1b, 1c). The optimized values of the lattice parameters of bulk Pt and of some of the most important parameters characterizing the Pt(110)-(2×1) surface (see Fig.1c) are presented in Table 1.

Compared with GGA DFs which overestimate the Pt lattice constant, the meta-GGA DFs (MS-PBEl, MS-RPBEl, MS-B86bl) yield more accurate lattice constants with an error in the range of 0.002~0.008 Å. The MS-PBEl-rVV10, MS-RPBEl-rVV10, and MS-B86bl-rVV10 DFs yield somewhat underestimated lattice constants when compared with experiment, but the values are more accurate than the ones obtained with PBE and RPBE. Among all DFs, MS-RPBEl and PBEsol show lattice parameters that are closest to the experimental value (3.913 Å), while the PBE-D3 value is also quite close. It is worth noting that the vdW-DF, vdW-DF2 and SPR32-vdW DFs significantly overestimate the lattice constant, all with values reaching more than 4 Å.

As Table 1 shows comparison of the more detailed structure of the surface as computed

with the various DFs shows the best agreement with the experimental LEED data.[99, 100] With the possible exception of the vdW-DF2 structure, all computed structures agree rather well with this experimental structure, and we speculate that this structure may be the most accurate experimental one. Our results also suggest that the tested DFs yield larger differences in the bulk lattice parameters than in the parameters characterizing the structure of the surface shown in Figure 1c and tabulated in Table 1, except of course in the value of the bulk interlayer spacing d_0, which is proportional to the bulk lattice parameter.

3.2 Methane adsorption

Since the ridge Pt atoms are most exposed to impinging molecules and they are the most undercoordinated, we will focus on the adsorption of methane on these sites, as in previous theoretical studies of methane DC on Pt(110)-(2×1).[43, 59, 61-64] The validity of this choice is confirmed by a recent experimental study, which found that the DC occurs mostly at ridge sites.[62] The stationary points characterizing the adsorption and transition state geometries may be labeled as K1, K2, L1, and L2, following Jackson and co-workers.[60]

Because the four corresponding adsorption configurations (see Figure 2) have roughly the same adsorption energy (*vide infra*), we focus on the K1 configuration to examine the performance of various DFs in describing methane adsorption. As displayed in Table 2, the PBE and RPBE DFs as well as the meta-GGA DFs yield a very small adsorption energy, which should be due to the lack of dispersion. The addition of the van der Waals interaction significantly increases E_{ads}. In particular, using rVV10 correlation instead of the correlation functional used with the ordinary MS meta-GGA DFs increases the well depth by values in the range 17 - 27 kJ/mol. It is well established that methane has a relatively strong physisorption well on Pt surfaces, with a consensus adsorption

energy of about 18 kJ/mol on Pt(111).[101]

3.3 Dissociation barrier and reaction energy

The DC dynamics is largely controlled by the corresponding barrier height. As reported in Ref. 49, the SRP32-vdW barrier heights (E_b) for the K1 and L2 configurations yielded a sticking probability curve that is shifted to higher energies by 19.3 kJ/mol on average from experiment. The calculated barriers were similar to those of Jackson and coworkers, who used the PBE DF.[60, 61] The underestimation of the experimental sticking probabilities suggest that the actual barrier height should be lower by about 19 kJ/mol. We have therefore searched for DFs that give an accurate description of the metal and yield barriers that are lower than the SRP32-vdW value by 10-25 kJ/mol.

In this section, reaction energy ($\triangle E$), activation energy without and with ZPE correction (E_a and E_a^{zpe}), the barrier height relative to gaseous CH_4 (E_b) are investigated with various DFs. Corresponding to the four modes of methane adsorption described in Sec. 3.2, there are also four methane dissociation TSs at the ridge (Figure 3), which are named as TS_{K1}, TS_{K2}, TS_{L1}, TS_{L2}, respectively. The corresponding FS structures can be found in Figure 4. In Table 2, the calculated E_a, E_a^{zpe}, E_b, and $\triangle E$ of the K1 configuration, as well as the corresponding TS geometry as defined in Figure 3, are presented. The value of E_a^{zpe} of all DFs is approximately 10 kJ/mol lower than E_a. The calculated reaction energy is in all cases positive, signaling an endoergic process, except for PBEsol. In addition, the length of the dissociating CH bond at the TS (d_{C-H}), the distance of the carbon to the surface at the TS (Z_C) and the angle between the dissociating C-H bond and the surface normal (φ) of TS_{K1} are also listed in the table, for which all DFs yielded similar values.

The SRP32-vdW barrier height measured from the gas-surface asymptote (E_b) computed for the K1 geometry is 65 kJ/mol, which means we are looking for DFs yielding barrier heights about 55-40 kJ/mol lower. From the table, it is clear that the PBEsol DF has the lowest E_a among all DFs with a value of 17.5 kJ/mol, which is physically unreasonable. Some of the DFs including the van der Waals interaction (PBE-D3, optB86b-vdW, TS and TS-SCS) likewise yield a barrier height that appears to be too low. On the other hand, vdW-DF, vdW-DF2, RPBE and BEEF-vdW yield too high energy barriers. These DFs are apparently inadequate for methane DC on Pt(110)-(2×1), based on the estimated range of barrier heights discussed above. The meta-GGA DFs likewise all yield barriers that are significantly higher than the estimated experimental barrier, but the addition of the rVV10 correction brings the barrier down to the range of the desired value for MS-PBEl-rVV10. Furthermore, the optPBE-vdW and optB88-vdW DFs also yield barrier heights that are in the "zone of confidence". In addition, the optPBE-vdW DF has been shown to have the lowest mean absolute deviations between experimental adsorption energies and theoretical ones for saturated hydrocarbons on Pt(111).[102] The PBE DF also yields a barrier height in the zone of confidence, but we do not explore this DF in AIMD calculations as earlier dynamics calculations based on this DF have consistently underestimated the measured sticking probability for the system of interest.[49]

Based on the calculated lattice constant, surface structure, adsorption energy, and dissociation barrier, we selected two DFs for the AIMD calculations: optPBE-vdW and MS-PBEl-rVV10. In Table 3, the adsorption energy, barrier height, reaction energy, and the geometry (as defined in Figure 3 and 4) are listed for the remaining three adsorption configurations, namely K2, L1 and L2, using the two DFs. It is clear from the table that the adsorption energy and barrier height vary only slightly with the adsorption configuration. We note that in all cases the L2 barrier

is lower than the K1 barrier by about 6 kJ/mol, as was also found in Ref. 49. We also note that the b_3 parameter (see Figure 1c) comes out somewhat lower with the optPBE-vdW and especially the MS-PBEl-rVV10 DF than with the SRP32-vdW DF. As discussed in Ref. 49, to which we refer for details, a lower b_3 parameter is correlated with a lower barrier height.

3.4 AIMD simulations of the dissociation dynamics

50 and 100 AIMD trajectories were calculated at two incidence energies using the initial conditions described in Sec. 2. Since the King and Wells method was used to measure the overall sticking probability, we do not distinguish between C-H and C-D bond cleavage in computing S_0. The calculated sticking probabilities are shown in Figure 5 where they are compared with experimental and previous theoretical results.[49] The calculated S_0 of CHD_3 excluding the trapped trajectories at the 124.6 kJ/mol incident energy, as obtained with the optPBE-vdW and MS-PBEl-rVV10 DFs, are 0.13±0.03 and 0.16±0.05, respectively. For 106.8 kJ/mol incident energy, the computed S_0 are 0.06±0.02 and 0.08±0.04, respectively. Only one trajectory was found to be trapped for E_i=124.6 kJ/mol with the optPBE-vdW DF. These computed sticking probabilities are significantly larger than the corresponding S_0 values obtained using the SRP-vdW DF, which are 0.060±0.008 and 0.047±0.007 for 124.6 and 106.8 kJ/mol incident energy, respectively, and in better agreement with the experimental values of 0.108±0.011 and 0.074±0.007.[49] The large error bounds of the AIMD results, which are computed based on the Monte Carlo sampling of the initial state of the trajectories (standard error $\sigma = \sqrt{p(1-p)/N_t}$, where p is the computed DC probability, and N_t is the number of AIMD trajectories used), are due to the small number of trajectories. However, the error bounds in the computed S_0 overlap with the experimental uncertainties. The larger sticking probabilities can be attributed to the lower DC barriers.

Furthermore, the MS-PBEl-rVV10 results are systematically higher than those obtained with the optPBE-vdW, which is consistent with the difference in the barrier heights.

Obviously, a quantitative comparison of the calculated S_0 with the experimental data is premature at this stage. A significantly larger number of trajectories is needed to lower the statistical uncertainty. This is difficult to achieve with the AIMD approach, especially with the meta-GGA DFs, because they typically require more computational resources. We plan to exploit recent developed machine learning strategies[58] to construct a high-dimensional PES to facilitate larger scale trajectory calculations in the future.

In Figure 6, the distribution of the initial projections of the center of mass positions of the incident CHD_3 are on the simulation unit cell are plotted for the two incident energies investigated, for the two DFs tested. It is clear that the majority of the reactive impacts (represented by the red dots) occurs near the ridge. This observation is consistent with previous theoretical investigations.[49] At these high energies, there is very little steering as the molecule approaches the surface, as evidenced by the small differences between the initial projections (solid red circles) and the impact sites, i.e., the projection at the point of reaction (when the reacting CH bond distance first becomes 2.2 Å, see the empty blue circles) of the reactive trajectories.

4. Conclusions

In this work, we have examined the performance of a number of DFs in describing the lattice of bulk Pt and the surface structure of the reconstructed Pt(110) with a missing row (Pt(110)-(2×1)), as well as the adsorption and dissociation of methane on this surface. The aim is to find a balanced description of both the metal surface geometry and the reactive molecule-metal surface interaction. Based on our results, we have identified three such DFs. The optPBE-vdW DF and the

optB88-vdW DFs consist of a GGA exchange DF, but a non-local van der Waals correlation DF. The MS-PBEl-rVV10 DF consists of a made-simple meta-GGA exchange DF and the rVV10 van der Waals correlation DF. The optPBE-vdW DF and the MS-PBEl-rVV10 DF have been used in AIMD calculations of the DC dynamics on Pt(110)-(2×1), and found to improve the agreement with the experimentally measured sticking probabilities over the earlier SRP32-vdW results. We attribute the better agreement to a more balanced characterization of the metal surface and the molecule-metal surface interaction. Both DFs yield values of the bulk lattice constant and the b_3 parameter that are in better agreement with experiment than the previous SRP32-vdW values, and lower barrier heights, as required for better agreement with the existing experiments.

The results reported in this work set the stage for the development of a high-dimensional PES for methane DC. Such a PES will require energy and gradient data along the DC pathways, which have been partially generated by the AIMD trajectories. Additional DFT calculations will probably be needed to cover a large coordinate space. With such an analytical PES, MD calculations can be carried out with much higher efficiency, which will permit a much larger number of trajectories. This will also enable the studies of the low energy regime where the precursor-mediated mechanism is operative. In this regime, AIMD would be extremely challenging because of the long residence time of the trapped trajectories, but the dynamics can still be readily handled with an analytical PES. A better understanding of the microscopic details of the DC dynamics under these industrially relevant conditions is expected to advance our knowledge of this important process.

Acknowledgements: F. W. and S. L. acknowledge financial support from the National Natural Science Foundation of China (Grant Nos. 21973013 and 21673040), the National Natural Science Foundation of Fujian Province, China (Grant No. 2020J02025), and the "Chuying Program" for the Top Young Talents of Fujian Province. E.W.F.S and G.-J. K. were supported financially through a NWO/CW TOP grant (Grant No. 715.017.001), and by a grant of supercomputer time from NWO Exacte en Natuurwetenschappen (NWO-ENW, Grant No. 2019.015). J.V. acknowledges support by the U.S. Department of Energy, Office of Science, Office of Basic Energy Sciences, Chemical Sciences, Geosciences, and Biosciences Division, Catalysis Science Program to the SUNCAT Center for Interface Science and Catalysis. H. G. thanks the National Science Foundation (Grant No. CHE-1951328) for support. We also thank Bin Jiang and Jun Chen for their technical help.

Table 1. Calculated geometric parameters for both the bulk Pt and the surface layers of Pt(110)-(2×1) with missing-row structure. The values of the lattice constant and of d_0 and b_3 are in Å. The values of Δd_{12}, Δd_{23}, and Δd_{34} are in % relative to d_0. The corresponding experimental values are included (LEED[99, 100], MEIS[103] and XRD[104]).

Functional	Lattice constant (a=b=c)	d_0	Δd_{12}	Δd_{23}	Δd_{34}	b_3
PBE	3.968	1.403	-20.03	-12.12	-11.83	0.346
PBE-D3	3.918	1.385	-19.57	-8.23	-10.25	0.300
optPBE-vdW	3.989	1.414	-21.07	-11.32	-12.02	0.350
optB86b-vdW	3.949	1.396	-19.84	-10.89	-11.25	0.319
optB88-vdW	3.977	1.406	-22.33	-11.81	-12.73	0.366
DF	4.030	1.425	-18.88	-7.86	-10.74	0.421
DF2	4.106	1.451	-24.95	-17.30	-15.23	0.388
TS	3.933	1.390	-19.42	-9.71	-10.94	0.323
TS-SCS	3.952	1.397	-20.11	-12.74	-12.10	0.332
PBEsol	3.914	1.384	-19.44	-11.42	-11.05	0.323
RPBE	3.991	1.411	-20.48	-12.26	-12.19	0.358
BEEF-vdW	3.993	1.412	-19.66	-10.73	-11.14	0.325
SRP32-vdW	4.020	1.422	-21.73	-11.88	-12.59	0.369
MS-PBEl	3.905	1.381	-20.93	-11.08	-11.44	0.325
MS-RPBEl	3.911	1.383	-20.39	-11.06	-11.28	0.322
MS-B86bl	3.908	1.383	-20.68	-11.42	-11.50	0.322
MS-PBEl-rVV10	3.879	1.372	-20.04	-9.18	-10.28	0.292
MS-RPBEl-rVV10	3.885	1.373	-19.16	-9.69	-10.27	0.300
MS-B86bl-rVV10	3.882	1.372	-19.68	-9.40	-10.35	0.297
LEED[99]	-	-	-17.4	-12.6	-8.7	0.32
LEED[100]	-	-	-18.5	1.1	0.4	0.17
MEIS[103]	-	-	-16 (3)	4 (3)	N/A	0.10
XRD[104]	3.912	-	-	-	-	-

Table 2. Methane adsorption energy without and with zero-point energy (ZPE) correction (E_{ads} and E_{ads}^{zpe}), reaction energy($\triangle E$), activation energy without and with ZPE correction (E_a and E_a^{zpe}), the barrier height relative to CH_4 in the gas phase (E_b), and parameters characterizing the K1 geometry of the TS for the first dehydrogenation of CH_4 on Pt(110)-(2×1) as calculated using various DFs for the surface geometry computed with these DFs. The values of E_{ads}, E_{ads}^{zpe}, ΔE, E_a, E_a^{zpe} and E_b are in kJ/mol. The values of d_{C-H} and Z_C are in Å. The value of φ is in degrees.

Functional	E_{ads}	E_{ads}^{zpe}	ΔE	E_a	E_a^{zpe}	E_b	d_{C-H}	Z_C	φ
PBE	-6.465	-3.859	19.394	60.689	51.137	54.225	1.543	2.201	128.5
PBE+D3	-24.893	-24.314	12.543	52.681	44.962	27.788	1.531	2.201	128.2
optPBE-vdw	-18.911	-16.788	27.209	72.557	63.294	53.646	1.565	2.224	128.6
optB86b-vdw	-21.323	-20.744	10.903	53.453	45.155	32.130	1.545	2.204	128.0
optB88-vdw	-19.972	-18.815	20.262	65.706	56.926	45.734	1.558	2.214	128.3
DF	-12.543	-7.526	49.111	104.880	93.301	92.336	1.579	2.281	130.5
DF2	-13.315	-9.649	46.023	93.494	82.688	80.179	1.610	2.240	128.8
TS	-21.999	-21.420	12.833	52.006	43.708	30.007	1.534	2.200	128.5
TS-SCS	-23.349	-21.516	17.560	54.900	45.445	31.551	1.544	2.198	129.3
PBEsol	-16.981	-16.113	-3.956	34.445	25.376	17.464	1.506	2.179	128.5
RPBE	-1.351	2.123	42.261	85.100	74.583	83.749	1.567	2.216	128.3
BEEF-vdW	-33.994	-29.213	43.708	88.863	77.913	54.869	1.563	2.219	129.5
SRP32-vdw	-19.394	-16.885	36.182	84.039	74.583	64.645	1.577	2.239	129.3
MS-PBEl	0.965	3.088	33.191	76.223	69.469	77.188	1.555	2.214	129.0
MS-RPBEl	5.693	8.587	35.893	78.057	69.373	83.749	1.550	2.219	130.1
MS-B86bl	3.473	6.079	35.314	77.864	69.855	81.337	1.553	2.216	129.6
MS-PBEl-rVV10	-15.824	-13.122	15.534	60.207	52.874	44.383	1.550	2.205	127.6
MS-RPBEl-rVV10	-20.937	-19.104	18.332	59.435	51.909	38.498	1.541	2.216	129.7
MS-B86bl-rVV10	-23.446	-21.227	16.981	58.567	50.269	35.121	1.542	2.214	129.5

Table 3. Methane adsorption energy without and with ZPE correction (E_{ads} and E_{ads}^{zpe}), reaction energy ($\triangle E$) and activation energy without and with ZPE (E_a and E_a^{zpe}), the barrier height relative to CH_4 in the gas phase (E_b) and parameters characterizing the K2, L1, and L2 geometries of the TS for the first dehydrogenation of CH_4 on Pt(110)-(2×1) as computed using the optPBE-vdW and MS-PBEl-rVV10 DFs, respectively. The values of E_{ads}, E_{ads}^{zpe}, ΔE, E_a, E_a^{zpe} and E_b are in kJ/mol. The values of d_{C-H} and Z_C are in Å. The value of φ is in degrees.

Functional	Pattern	E_{ads}	E_{ads}^{zpe}	ΔE	E_a	E_a^{zpe}	E_b	d_{C-H}	Z_C	φ
optPBE-vdW	K2	-18.815	-17.464	25.086	75.259	65.706	56.444	1.543	2.245	130.2
	L1	-19.394	-17.367	33.384	66.671	59.145	47.278	1.587	2.139	118.3
	L2	-19.972	-16.885	31.647	66.285	58.374	46.313	1.560	2.158	119.5
MS-PBEl-rVV10	K2	-15.920	-12.640	11.868	63.487	54.032	47.567	1.512	2.236	131.1
	L1	-16.499	-13.411	17.753	53.742	48.050	37.243	1.565	2.117	117.3
	L2	-17.657	-13.315	16.017	53.839	47.085	36.182	1.532	2.114	116.2

TOC graphic：

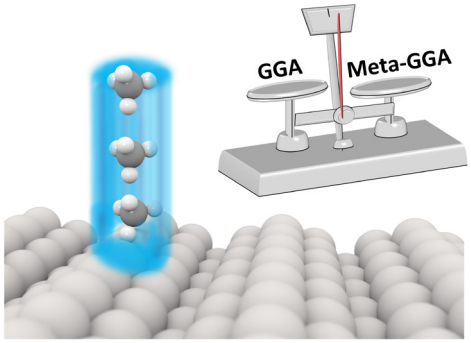

References:

1. L. B. F. Juurlink, D. R. Killelea and A. L. Utz, Prog. Surf. Sci. **84**, 69 (2009).
2. H. Chadwick and R. D. Beck, Annu. Rev. Phys. Chem. **68**, 39 (2017).
3. S. Nave, A. K. Tiwari and B. Jackson, J. Phys. Chem. A **118**, 9615 (2014).
4. B. Jiang and H. Guo, J. Chem. Phys. **150**, 180901 (2019).
5. G.-J. Kroes, Phys. Chem. Chem. Phys. **23**, 8962 (2021).
6. C. T. Rettner, H. E. Pfnur and D. J. Auerbach, Phys. Rev. Lett. **54**, 2716 (1985).
7. M. B. Lee, Q. Y. Yang and S. T. Ceyer, J. Chem. Phys. **87**, 2724 (1987).
8. A. C. Luntz and D. S. Bethune, J. Chem. Phys. **90**, 1274 (1989).
9. P. M. Holmblad, J. Wambach and I. Chorkendorff, J. Chem. Phys. **102**, 8255 (1995).
10. L. B. F. Juurlink, P. R. MaCabe, R. R. Smith, C. L. DeCologero and A. L. Utz, Phys. Rev. Lett. **83**, 868 (1999).
11. R. D. Beck, P. Maroni, D. C. Papageorgopoulos, T. T. Dang, M. P. Schmid and T. R. Rizzo, Science **302**, 98 (2003).
12. R. R. Smith, D. R. Killelea, D. F. DelSesto and A. L. Utz, Science **304**, 992 (2004).
13. L. B. F. Juurlink, R. R. Smith, D. R. Killelea and A. L. Utz, Phys. Rev. Lett. **94**, 208303 (2005).
14. P. Maroni, D. C. Papageorgopoulos, M. Sacchi, T. T. Dang, R. D. Beck and T. R. Rizzo, Phys. Rev. Lett. **94**, 246104 (2005).
15. D. R. Killelea, V. L. Campbell, N. S. Shuman and A. L. Utz, Science **319**, 790 (2008).
16. A. K. Tiwari, S. Nave and B. Jackson, Phys. Rev. Lett. **103**, 253201 (2009).
17. S. Nave and B. Jackson, Phys. Rev. B **81**, 233408 (2010).
18. B. Jackson and S. Nave, J. Chem. Phys. **135**, 114701 (2011).
19. M. Sacchi, D. J. Wales and S. J. Jenkins, J. Phys. Chem. C **115**, 21832 (2011).
20. B. Jackson and S. Nave, J. Chem. Phys. **138**, 174705 (2013).
21. M. Mastromatteo and B. Jackson, J. Chem. Phys. **139**, 194701 (2013).
22. X. J. Shen, A. Lozano, W. Dong, H. F. Busnengo and X. H. Yan, Phys. Rev. Lett. **112**, 046101 (2014).
23. F. Nattino, H. Ueta, H. Chadwick, M. E. van Reijzen, R. D. Beck, B. Jackson, M. C. van Hemert and G.-J. Kroes, J. Phys. Chem. Lett. **5**, 1294 (2014).
24. H. Guo and B. Jackson, J. Phys. Chem. C **119**, 14769 (2015).
25. X. Shen, Z. Zhang and D. H. Zhang, Phys. Chem. Chem. Phys. **17**, 25499 (2015).
26. X. Shen, Z. Zhang and D. H. Zhang, J. Chem. Phys. **144**, 101101 (2016).
27. H. Guo and B. Jackson, J. Chem. Phys. **144**, 184709 (2016).
28. X. Shen, Z. Zhang and D. H. Zhang, J. Phys. Chem. C **120**, 20199 (2016).
29. R. Moiraghi, A. Lozano and H. F. Busnengo, J. Phys. Chem. C **120**, 3946 (2016).
30. F. Nattino, D. Migliorini, M. Bonfanti and G.-J. Kroes, J. Chem. Phys. **144**, 044702 (2016).
31. F. Nattino, D. Migliorini, G.-J. Kroes, E. Dombrowski, E. A. High, D. R. Killelea and A. L. Utz, J. Phys. Chem. Lett. **7**, 2402 (2016).
32. D. Migliorini, H. Chadwick, F. Nattino, A. Gutiérrez-González, E. Dombrowski, E. A. High, H. Guo, A. L. Utz, B. Jackson, R. D. Beck and G.-J. Kroes, J. Phys. Chem. Lett. **8**, 4177 (2017).
33. X. Shen, Z. Zhang and D. H. Zhang, J. Chem. Phys. **147**, 024702 (2017).
34. X. Zhou, F. Nattino, Y. Zhang, J. Chen, G.-J. Kroes, H. Guo and B. Jiang, Phys. Chem. Chem. Phys. **19**, 30540 (2017).
35. D. Migliorini, H. Chadwick and G.-J. Kroes, J. Chem. Phys. **149**, 094701 (2018).
36. H. Chadwick, A. Gutiérrez-González, R. D. Beck and G.-J. Kroes, J. Phys. Chem. C **123**, 14530 (2019).
37. N. Gerrits, K. Shakouri, J. Behler and G.-J. Kroes, J. Phys. Chem. Lett. **10**, 1763 (2019).
38. X. Zhou, B. Jiang and H. Guo, J. Phys. Chem. C **123**, 20893 (2019).
39. H. Guo and B. Jackson, J. Chem. Phys. **150**, 204703 (2019).
40. B. Jackson, J. Chem. Phys. **153**, 034704 (2020).
41. R. Moiraghi, A. Lozano, E. Peterson, A. Utz, W. Dong and H. F. Busnengo, J. Phys. Chem. Lett. **11**, 2211 (2020).
42. X. Zhou, Y. Zhang, H. Guo and B. Jiang, Phys. Chem. Chem. Phys. **23**, 4376 (2021).
43. H. Chadwick, A. Gutiérrez-González, D. Migliorini, R. D. Beck and G.-J. Kroes, J. Phys. Chem. C **122**, 19652 (2018).
44. C. Díaz, E. Pijper, R. A. Olsen, H. F. Busnengo, D. J. Auerbach and G.-J. Kroes, Science **326**, 832 (2009).

45. J. P. Perdew, J. A. Chevary, S. H. Vosko, K. A. Jackson, M. R. Pederson, D. J. Singh and C. Fiolhais, Phys. Rev. B **46**, 6671 (1992).
46. J. P. Perdew, K. Burke and M. Ernzerhof, Phys. Rev. Lett. **77**, 3865 (1996).
47. B. Hammer, L. B. Hansen and J. K. Nørskov, Phys. Rev. B **59**, 7413 (1999).
48. M. Dion, H. Rydberg, E. Schröder, D. C. Langreth and B. I. Lundqvist, Phys.Rev.Lett. **92**, 246401 (2004).
49. H. Chadwick, A. Gutiérrez-González, R. D. Beck and G.-J. Kroes, J. Chem. Phys. **150**, 124702 (2019).
50. H. Chadwick, H. Guo, A. Gutiérrez-González, J. P. Menzel, B. Jackson and R. D. Beck, J. Chem. Phys. **148**, 014701 (2018).
51. A. Mondal, M. Wijzenbroek, M. Bonfanti, C. Díaz and G.-J. Kroes, J. Phys. Chem. A **117**, 8770 (2013).
52. A. Marashdeh, S. Casolo, L. Sementa, H. Zacharias and G.-J. Kroes, J. Phys. Chem. C **117**, 8851 (2013).
53. A. V. Walker and D. A. King, Phys. Rev. Lett. **82**, 5156 (1999).
54. A. V. Walker and D. A. King, J. Chem. Phys. **112**, 4739 (2000).
55. D. C. Seets, C. T. Reeves, B. A. Ferguson, M. C. Wheeler and C. B. Mullins, J. Chem. Phys **107**, 10229 (1997).
56. D. C. Seets, M. C. Wheeler and C. B. Mullins, J. Chem. Phys. **107**, 3986 (1997).
57. E. Dombrowski, E. Peterson, D. Del Sesto and A. L. Utz, Catal. Today **244**, 10 (2015).
58. B. Jiang, J. Li and H. Guo, J. Phys. Chem. Lett. **11**, 5120 (2020).
59. A. T. Anghel, D. J. Wales, S. J. Jenkins and D. A. King, Phys. Rev. B **71**, 113410 (2005).
60. S. Nave, A. K. Tiwari and B. Jackson, J. Chem. Phys. **132**, 054705 (2010).
61. D. Han, S. Nave and B. Jackson, J. Phys. Chem. A **117**, 8651 (2013).
62. A. Gutiérrez-González, M. E. Torio, H. F. Busnengo and R. D. Beck, Top. Catal. **62**, 859 (2019).
63. I. F. Peludhero, A. Gutiérrez-González, W. Dong, R. D. Beck and H. F. Busnengo, J. Phys. Chem. C **125**, 11904 (2021).
64. L. Schimka, J. Harl, A. Stroppa, A. Grüneis, M. Marsman, F. Mittendorfer and G. Kresse, Nat. Mat. **9**, 741 (2010).
65. J. P. Perdew, MRS Bull. **38**, 743 (2013).
66. J. Sun, B. Xiao and A. Ruzsinszky, J. Chem. Phys. **137**, 051101 (2012).
67. J. Sun, R. Haunschild, B. Xiao, I. W. Bulik, G. E. Scuseria and J. P. Perdew, J. Chem. Phys. **138**, 044113 (2013).
68. F. Della Sala, E. Fabiano and L. A. Constantin, Inter. J. Quantum Chem. **116**, 1641 (2016).
69. J. Wellendorff, K. T. Lundgaard, A. Møgelhøj, V. Petzold, D. D. Landis, J. K. Nørskov, T. Bligaard and K. W. Jacobsen, Phys. Rev. B **85**, 235149 (2012).
70. K. T. Lundgaard, J. Wellendorff, J. Voss, K. W. Jacobsen and T. Bligaard, Phys. Rev. B **93**, 235162 (2016).
71. S. Mallikarjun Sharada, R. K. B. Karlsson, Y. Maimaiti, J. Voss and T. Bligaard, Phys. Rev. B **100**, 035439 (2019).
72. K. Brown, Y. Maimaiti, K. Trepte, T. Bligaard and J. Voss, J. Comput. Chem. **42**, 2004 (2021).
73. F. Tran, J. Stelzl and P. Blaha, J. Chem. Phys. **144**, 204120 (2016).
74. S. Mallikarjun Sharada, T. Bligaard, A. C. Luntz, G.-J. Kroes and J. K. Nørskov, J. Phys. Chem. C **121**, 19807 (2017).
75. E. W. F. Smeets, J. Voss and G.-J. Kroes, J. Phys. Chem. A **123**, 5395 (2019).
76. J. P. Perdew, A. Ruzsinszky, G. I. Csonka, O. A. Vydrov, G. E. Scuseria, L. A. Constantin, X. Zhou and K. Burke, Phys. Rev. Lett. **100**, 136406 (2008).
77. N. Gerrits, J. Geweke, E. W. F. Smeets, J. Voss, A. M. Wodtke and G.-J. Kroes, J. Phys. Chem. C **124**, 15944 (2020).
78. N. Gerrits, E. W. F. Smeets, S. Vuckovic, A. D. Powell, K. Doblhoff-Dier and G.-J. Kroes, J. Phys. Chem. Lett. **11**, 10552 (2020).
79. E. W. F. Smeets and G.-J. Kroes, J. Phys. Chem. C **125**, 8993 (2021).
80. O. A. Vydrov and T. Van Voorhis, J. Chem. Phys. **133**, 244103 (2010).
81. R. Sabatini, T. Gorni and S. de Gironcoli, Phys. Rev. B **87**, 041108 (2013).
82. J. Klimeš, D. R. Bowler and A. Michaelides, J. Phys.: Condens. Matter **22**, 022201 (2010).
83. J. Klimeš, D. R. Bowler and A. Michaelides, Phys. Rev. B **83**, 195131 (2011).
84. M. Wijzenbroek, D. M. Klein, B. Smits, M. F. Somers and G.-J. Kroes, J. Phys. Chem. A **119**, 12146 (2015).
85. L. Zhu, Y. Zhang, L. Zhang, X. Zhou and B. Jiang, Phys. Chem. Chem. Phys. **22**, 13958 (2020).
86. G. Kresse and J. Furthmuller, Comp. Mater. Sci. **6**, 15 (1996).
87. G. Kresse and J. Furthmuller, Phys. Rev. B **54**, 11169 (1996).
88. G. Kresse and D. Joubert, Phys. Rev. B **59**, 1758 (1999).

89. P. E. Blöchl, Phys. Rev. B **50**, 17953 (1994).
90. H. J. Monkhorst and J. D. Pack, Phys. Rev. B **13**, 5188 (1976).
91. G. Henkelman, B. P. Uberuaga and H. Jónsson, J. Chem. Phys. **113**, 9901 (2000).
92. S. Grimme, J. Antony, S. Ehrlich and H. Krieg, J. Chem. Phys. **132**, 154104 (2010).
93. K. Lee, É. D. Murray, L. Kong, B. I. Lundqvist and D. C. Langreth, Phys. Rev. B **82**, 081101 (2010).
94. A. Tkatchenko and M. Scheffler, Phys. Rev. Lett. **102**, 073005 (2009).
95. T. Bučko, S. Lebègue, J. Hafner and J. G. Ángyán, Phys. Rev. B **87**, 064110 (2013).
96. B. Jiang and H. Guo, J. Phys. Chem. C **117**, 16127 (2013).
97. X. Hu, W. L. Hase and T. Pirraglia, J. Comput. Chem. **12**, 1014 (1991).
98. J. I. Lee, W. Mannstadt and A. J. Freeman, Phys. Rev. B **59**, 1673 (1999).
99. E. C. Sowa, M. A. Van Hove and D. L. Adams, Surf. Sci. **199**, 174 (1988).
100. P. Fery, W. Moritz and D. Wolf, Phys. Rev. B **38**, 7275 (1988).
101. K. Watanabe and Y. Matsumoto, Surf. Sci. **390**, 250 (1997).
102. S. Gautier, S. N. Steinmann, C. Michel, P. Fleurat-Lessard and P. Sautet, Phys. Chem. Chem. Phys. **17**, 28921 (2015).
103. P. Fenter and T. Gustafsson, Phys. Rev. B **38**, 10197 (1988).
104. W. P. Davey, Phys. Rev. **25**, 753 (1925).

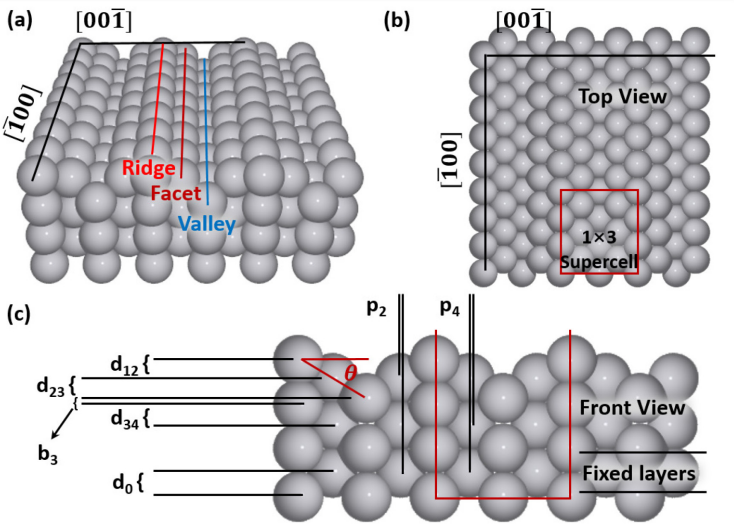

Figure 1. (a) The geometry of the Pt(110)-(2×1) surface with the ridge, facet and valley, and the top (b) and side views (c). The geometric parameters for the atom inter-layer spacing are given in (c): $d_{i,i+1}$ denotes the (average) inter-layer spacing and d_0 denotes the ideal bulk interlayer spacing, while p_i and b_i denote the lateral pairing and buckling in layer i, respectively. θ denotes the angle between the normal of the facet and the normal of surface.

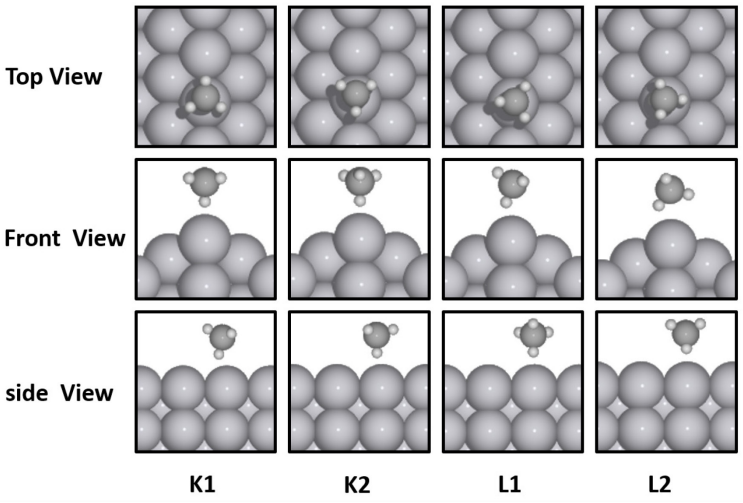

Figure 2. Top, front and side views of the CH_4 adsorption structure on the ridge of Pt(110)- (2×1).

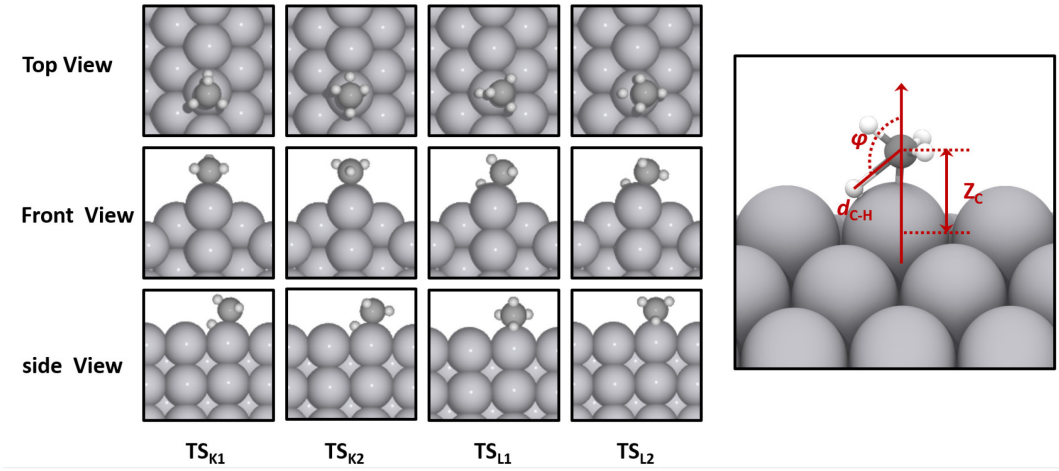

Figure 3. Top, front and side views of the TS structure for CH_4 dissociation for the K1, K2, L1, L2 configurations on the ridge of the Pt(110)-(2×1) surface. d_{C-H} denotes the length of the breaking C-H bond of TS. Z_C is the vertical distance between the C atom and the ridge Pt atom. φ denotes the angle between the breaking C-H bond and the normal of surface.

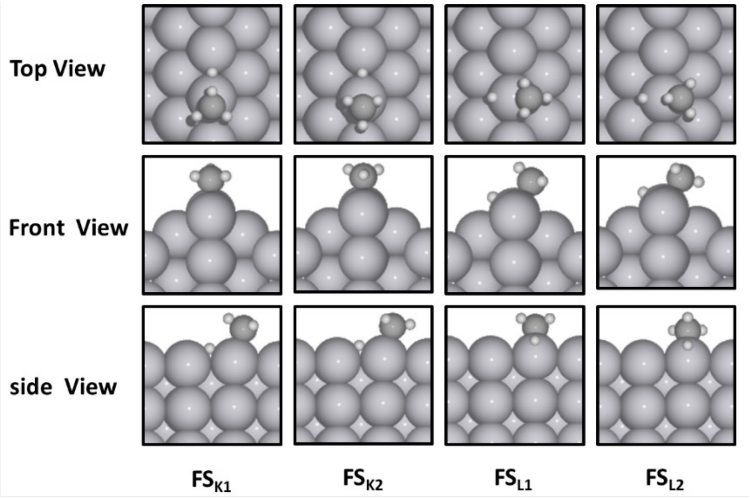

Figure 4. Top, front and side views of the FS structure for CH_4 dissociation for the K1, K2, L1, L2 configurations on the ridge of the Pt(110)-(2×1) surface.

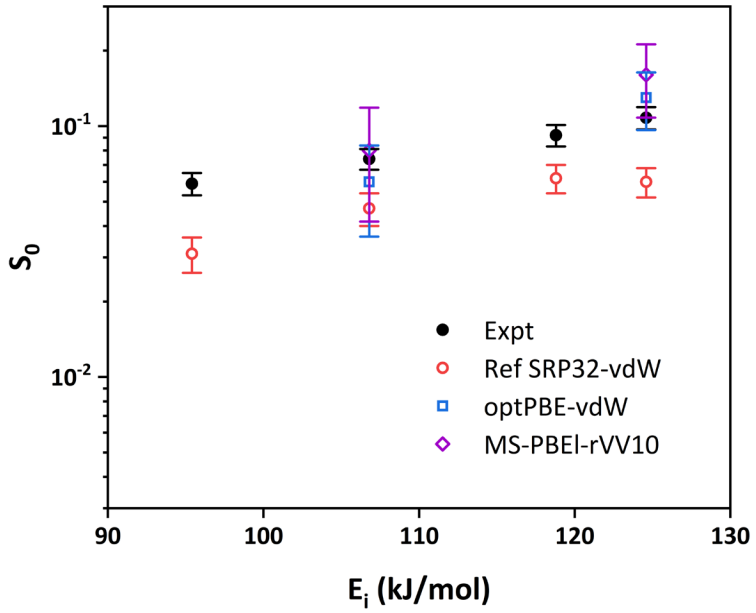

Figure 5. Comparison of the experimental sticking coefficients with those from AIMD simulations using the SPR32-vdW (excluding the trapped trajectories),[49] optPBE-vdW and MS-PBEl-rVV10 DFs for CHD_3 dissociation at 650 K $T_{surface}$.

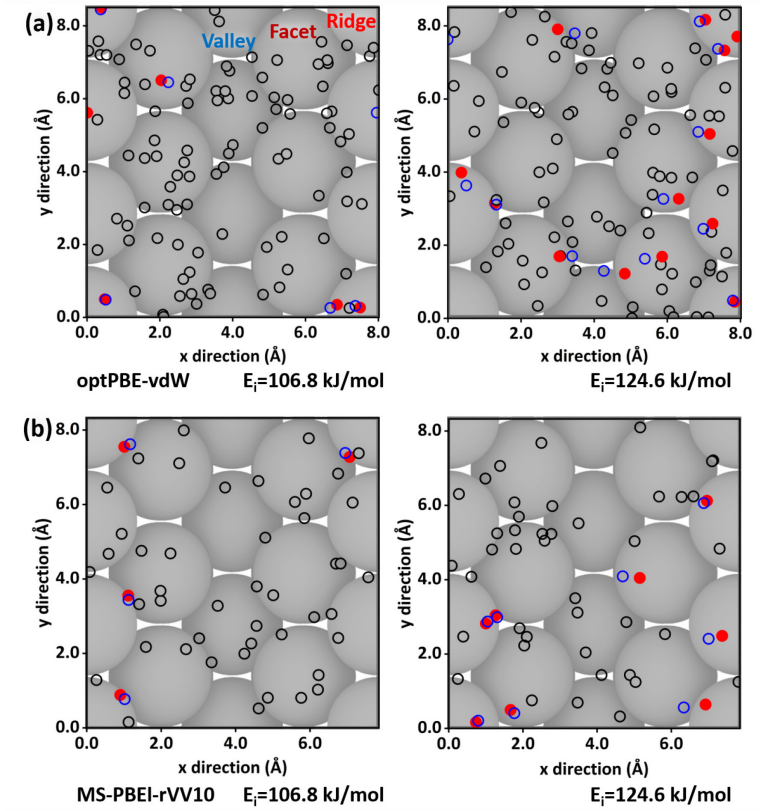

Figure 6. Distributions of the initial CHD_3 center of mass positions in the unit cell using the optPBE-vdW and MS-PBEl-rVV10 DFs at two incident energies, with the red dots representing the reactive ones. The blue dots are the corresponding impact positions of these reactive trajectories, which are not far from the corresponding red dots, indicating small steering effects.